

# Machine Learning-Driven High-Precision Model for $\alpha$ -Decay Energy and Half-Life Prediction of superheavy nuclei

Qingning Yuan<sup>1</sup>, Panpan Qi<sup>1</sup>, Xuanpen Xiao<sup>1</sup>, Xue Wang, Juan He<sup>1</sup>, Guimei Long<sup>1</sup>, Zhengwei Duan<sup>1</sup>, Yangyan Dai<sup>1</sup>, Runchao Yan<sup>1</sup>, Gongming Yu<sup>1</sup>, Haitao Yang<sup>2</sup>, Qiang Hu<sup>3</sup>

<sup>1</sup>College of Physics and Technology, Kunming University, Kunming 650214, China

<sup>2</sup>College of Science, Zhaotong University, Zhaotong 657000, China

<sup>3</sup>Institute of Modern Physics, Chinese Academy of Sciences, Lanzhou 730000, China

Email: yuan\_QN@163.com, qipanpan1999@163.com, xxp232316@163.com, 15752029336@139.com, 19223878519@139.com, 15912196629@163.com, 14787598564@163.com, m18288970135@163.com, m18608829713@163.com, ygmanan@kmu.edu.cn, yanghaitao205@163.com, qianghu@impcas.ac.cn

Based on Extreme Gradient Boosting (XGBoost) framework optimized via Bayesian hyperparameter tuning, we investigated the  $\alpha$ -decay energy and half-life of superheavy nuclei. By incorporating key nuclear structural features-including mass number, proton-to-neutron ratio, magic number proximity, and angular momentum transfer-the optimized model captures essential physical mechanisms governing  $\alpha$ -decay. On the test set, the model achieves significantly lower mean absolute error (MAE) and root mean square error (RMSE) compared to empirical models such as Royer and Budaca, particularly in the low-energy region. SHapley Additive exPlanations (SHAP) analysis confirms these mechanisms are dominated by decay energy, angular momentum barriers, and shell effects. This work establishes a physically consistent, data-driven tool for nuclear property prediction and offers valuable insights into  $\alpha$ -decay processes from a machine learning perspective.

**Key words:**  $\alpha$ -decay, Decay energy, Machine learning

**PACS:** 23.60.+e, 23.70.+j

---

## I. INTRODUCTION

Alpha decay represents one of the earliest discovered phenomena in radioactive decay, with scientific investigation dating back to the late 19th century. In 1899, Rutherford and collaborators first identified alpha particle emissions in their pioneering studies of uranium radiation. Later, through systematic experiments in 1909, they conclusively determined these emitted particles to be helium nuclei-a landmark discovery that established the experimental cornerstone for nuclear structure research [1-3]. Consequently,  $\alpha$ -decay emerged not only as a pivotal research domain in early nuclear physics but also established fundamental theoretical foundations for elucidating nuclear structure configurations and subatomic interaction mechanisms. Later, through systematic analysis of experimental data, Geiger and Nuttall (1911) identified a distinct correlation between  $\alpha$ -decay half-life and disintegration energy.

This discovery enabled them to formulate the foundational empirical relationship now known as the Geiger-Nuttall law, which quantitatively describes the logarithmic-linear dependence of nuclear half-life on decay energy release. This seminal correlation established critical theoretical foundations that facilitated the refinement of phenomenological models for radioactive decay processes, ultimately advancing precise characterization of nuclear disintegration dynamics [4].

With the advancement of quantum mechanical formalism, Gamow (1928) proposed the seminal quantum tunneling theory, establishing the essential theoretical framework linking  $\alpha$ -decay processes to quantum tunneling phenomena. This paradigm-shifting work systematically explained both the  $\alpha$ -particle emission mechanism and its characteristic exponential half-life dependence through first-principles quantum analysis, thereby providing rigorous theoretical substantiation for Geiger and Nuttall's empirical observations [5]. Building upon this theoretical foundation, researchers have developed numerous empirical formulas to calculate the logarithm of nuclear half-life. Several widely adopted formulations-including the Budaca formula, the Royer formula, and the Universal Decay Law (UDL)-have gained significant prominence. Continuous refinements based on theoretical advances and experimental data have enhanced these models' accuracy across broad nuclear domains, collectively advancing nuclear physics research [6-11]. Although these empirical formulas account for nucleon parity and employ distinct parameter sets for different nuclear categories, they frequently demonstrate systematic deviations in low-energy regions or for nuclei far from the valley of stability. This limitation stems primarily from their empirical parameters being derived from experimental data heavily concentrated near the stability line and in regions of higher  $\alpha$ -decay energies ( $Q_\alpha$ ). Conversely, for nuclei in low- $Q_\alpha$  or exotic regions, sparse experimental data-often with substantial uncertainties-limit model reliability and generalizability. Furthermore, lower  $Q_\alpha$  values correspond to dramatically reduced penetration probabilities, which exhibit exponential sensitivity to  $Q_\alpha$  variations. Consequently, even minor  $Q_\alpha$  fluctuations can cause orders-of-magnitude discrepancies in half-life predictions. Moreover, the simplified treatment of potential barriers and tunneling dynamics in these empirical approaches, while effective near fitted regions, introduces amplified errors at lower energies, thereby magnifying systematic discrepancies [12-14].

Recent advances in computer technology have dramatically expanded capabilities in data processing and analysis, propelling the adoption of machine learning across scientific disciplines. In physics-a field dedicated to uncovering matter's fundamental nature and universal laws-machine learning is increasingly recognized as a powerful tool for solving complex problems. Traditional physics approaches typically combine mathematical modeling, experimental observation, and numerical simulation. However, when addressing high-dimensional phase spaces, multiscale systems, or strongly correlated phenomena, these conventional methods face bottlenecks including prohibitive computational costs and the absence of accurate theoretical frameworks. Consequently, both predictive accuracy and model generalizability become fundamentally constrained [15-19]. To overcome these limitations, machine learning (ML) has been increasingly applied to model nuclear decay properties, particularly  $\alpha$ -decay. Various ML algorithms-including artificial neural networks (ANN), support vector machines (SVM), Gaussian processes (GP), and gradient boosting methods such as XGBoost-have demonstrated notable success in predicting  $\alpha$ -decay energies and half-lives. These approaches effectively capture complex nonlinear relationships between nuclear structural features and decay

observables, frequently surpassing traditional empirical formulas, especially for low-decay-energy regions and exotic nuclei [20-24].

Despite significant advances in nuclear decay modeling, most existing machine learning approaches remain constrained by limited precision control and vulnerability to over/underfitting. Moreover, systematic comparisons with classical empirical formulas across energy regimes are still insufficient, while model interpretability requires further enhancement.

Furthermore, high-quality experimental data remain inherently scarce for exotic nuclei—particularly those far from the valley of stability or in low decay-energy regions. This scarcity challenges both empirical modeling and the development of robust, generalizable data-driven approaches. Consequently, developing models capable of accurate predictions with physical consistency under limited data conditions becomes imperative.

To address these challenges, this study introduces an integrated and interpretable machine learning framework for simultaneous prediction of  $\alpha$ -decay energy and half-life. Built using the XGBoost regression algorithm, the model incorporates physically meaningful nuclear structure features including mass number, proton-to-neutron ratio, shell proximity (magic number distance), and angular momentum transfer. Bayesian hyperparameter optimization enhances model stability and predictive accuracy. Performance is rigorously evaluated against traditional empirical formulas (Royer and Budaca) across training and test sets, with SHAP-based feature attribution employed to elucidate the underlying physical mechanisms governing  $\alpha$ -decay.

This paper is organized as follows: In section II, we present  $\alpha$ -decay energy and half-life of superheavy nuclei in Extreme Gradient Boosting (XGBoost) framework optimized via Bayesian hyperparameter tuning. The results for  $\alpha$ -decay energy and half-life of superheavy nuclei are represented in Sec.III. Finally, the conclusion is given in Sec.IV.

## II. GENERAL FORMALISM

This section details our systematic modeling workflow, comprising mathematical fundamentals of XGBoost, bayesian hyperparameter optimization, feature engineering, model parameter analysis, empirical formula benchmarking. The experimental dataset, sourced from Refs. [25-27], undergoes appropriate preprocessing before being utilized for both machine learning training and empirical formula validation.

Alpha decay—a quantum tunneling process in radioactive decay—occurs when an  $\alpha$ -particle penetrates the nuclear potential barrier to escape the parent nucleus. The decay half-life is described within Gamow theory, which employs the Wentzel-Kram-Brillouin (WKB) approximation to calculate the quantum tunneling probability. In the standard WKB formalism, after preformation inside the parent nucleus, the  $\alpha$ -particle tunnels through an effective potential barrier comprising nuclear attraction, Coulomb repulsion, and centrifugal components. The tunneling probability is primarily governed by the Gamow factor derived through the WKB approximation [14,28-29]

$$P = \exp\left(-\frac{2}{\hbar} \int_{R_{\text{in}}}^{R_{\text{out}}} \sqrt{2\mu|V(r) - Q_\alpha|} \, dr\right), \quad (1)$$

where  $\mu$  is the reduced mass,  $V(r)$  is the potential energy function,  $Q_\alpha$  is the decay energy, and  $R_{\text{in}}$  and  $R_{\text{out}}$  are the classical turning points. This formulation explicitly reveals the critical role of decay energy ( $Q_\alpha$ ) in governing tunneling probability and consequently decay half-life through its exponential dependence.

Following Ref. [14], the  $\alpha$ -decay half-life is given by

$$T_{1/2} = \frac{\ln 2}{\lambda} = \frac{\ln 2}{\nu S_c P}, \quad (2)$$

where  $\lambda$  denotes the decay constant,  $\nu$  is the assault frequency, and  $P$  is the tunneling probability. As equations (1) and (2) demonstrate, even slight variations in input parameters can cause orders-of-magnitude changes in the calculated half-life. Crucially, since the penetration probability  $P$  depends exponentially on the decay energy  $Q_\alpha$ , any uncertainty in  $Q_\alpha$  introduces a strong exponential uncertainty into the predicted half-life [30-31].

Moreover, since  $\alpha$ -decay half-lives often span several orders of magnitude, this wide range poses substantial challenges for data modeling and regression prediction. To improve the numerical stability of the machine learning model and mitigate the influence of extreme values, the present study employs the base-10 logarithm of the half-life ( $\log_{10} T_{1/2}$ ) as the target variable for regression [32-33].

## 2.1 The Mathematical Fundamentals of XGBoost

We first present the mathematical formulation of the XGBoost model. The prediction output of XGBoost can be expressed as [34]

$$\hat{y}_i = \phi(x_i) = \sum_{k=1}^K f_k(x_i), \quad f_k \in \mathcal{F}. \quad (3)$$

Here,  $\hat{y}_i$  denotes the predicted value for the  $i^{\text{th}}$  sample,  $K$  is the total number of decision trees, and  $f_k(x_i)$  represents the function learned by the  $k^{\text{th}}$  tree for the input  $x_i$ . The model  $F$  consists of all possible regression trees, each tree is defined as  $f(x) = w_{q(x)}$ ,  $q: \mathbb{R}^m \rightarrow \{1, 2, \dots, T\}$ . Each new tree is added to correct the residuals generated by the previous trees. The training process from the initial tree up to the  $K^{\text{th}}$  tree can be formalized as [35]

$$\begin{aligned} \hat{y}_i^{(0)} &= f_0(x_i) = 0 \\ \hat{y}_i^{(1)} &= f_0(x_i) + f_1(x_i) = \hat{y}_i^{(0)} + f_1(x_i) \\ \hat{y}_i^{(2)} &= f_0(x_i) + f_1(x_i) + f_2(x_i) = \hat{y}_i^{(1)} + f_2(x_i) \end{aligned} \quad (4)$$

.....

$$\hat{y}_i^{(n)} = \sum_{k=1}^K f_k(x_i) = \hat{y}_i^{(K-1)} + f_K(x_i).$$

To prevent overfitting, a regularization term  $\sum_k \Omega(f_k)$  is introduced [36]

$$\mathcal{L}(\phi) = \sum_i l(y_i, \hat{y}_i) + \sum_k \Omega(f_k), \quad (5)$$

within this framework, the first term in equations (5) corresponds to the prediction-error loss functional, whose mathematical representation is given by

$$\Omega(f) = \gamma T + \frac{1}{2} \lambda \sum_{j=1}^T w_j^2, \quad (6)$$

here, the first term penalizes the addition of new leaves, while the second term represents the L2 regularization term, which controls model complexity. Based on Equation (5), assuming a new tree  $f_t$  is to be added at the  $t$ -th iteration, the objective function to be minimized can be expressed as[37-38]

$$\mathcal{L}^{(t)} = \sum_{i=1}^n l(y_i, \hat{y}_i^{(t-1)} + f_t(x_i)) + \Omega(f_t), \quad (7)$$

since  $f_t$  is a tree-structured function in function space, direct optimization is challenging. Therefore, we approximate the objective using a Taylor expansion. Specifically, we expand the loss function with respect to the newly introduced function  $f_t(x_i)$  at the  $t$ -th iteration as follows:

$$l(y_i, \hat{y}_i^{(t-1)} + f_t(x_i)) \approx l(y_i, \hat{y}_i^{(t-1)}) + g_i f_t(x_i) + \frac{1}{2} h_i f_t(x_i)^2, \quad (8)$$

where  $g_i = \frac{\partial l(y_i, \hat{y}_i)}{\partial \hat{y}_i} \Big|_{\hat{y}_i^{(t-1)}}$ ,  $h_i = \frac{\partial^2 l(y_i, \hat{y}_i)}{\partial \hat{y}_i^2} \Big|_{\hat{y}_i^{(t-1)}}$ . Since our optimization target is  $f_t$ ,

we can omit the terms that are independent of  $f_t$ . Therefore, the objective simplifies to

$$\tilde{\mathcal{L}}^{(t)} = \sum_{i=1}^n \left[ g_i f_t(x_i) + \frac{1}{2} h_i f_t(x_i)^2 \right] + \Omega(f_t), \quad (9)$$

since  $f(x) = w_{q(x)}$ ,  $q: \mathbb{R}^m \rightarrow \{1, 2, \dots, T\}$ , the sample set assigned to the  $j^{th}$  leaf is defined as

$$I_j = \{i | q(x_i) = j\}, \quad (10)$$

by regrouping all samples according to their corresponding leaf nodes and rewriting Equation (9), we obtain

$$\tilde{\mathcal{L}}^{(t)} = \sum_{j=1}^T \left[ \sum_{i \in I_j} \left( g_i w_j + \frac{1}{2} h_i w_j^2 \right) \right] + \gamma T + \frac{1}{2} \lambda \sum_{j=1}^T w_j^2, \quad (11)$$

where  $w_j$  denotes the score of the  $j^{th}$  leaf, and  $T$  represents the total number of leaves in the tree. By factoring out common terms, we obtain

$$\tilde{\mathcal{L}}^{(t)} = \sum_{j=1}^T \left[ G_j w_j + \frac{1}{2} (H_j + \lambda) w_j^2 \right] + \gamma T, \quad (12)$$

where  $G_j = \sum_{i \in I_j} g_i$ ,  $H_j = \sum_{i \in I_j} h_i$ , next, we take the derivative of  $w_j$  and set it to zero:

$$\frac{\partial \tilde{\mathcal{L}}^{(t)}}{\partial w_j} = G_j + (H_j + \lambda) w_j = 0, \quad (13)$$

the solution can be obtained

$$w_j^* = -\frac{G_j}{H_j + \lambda}, \quad (14)$$

If the gradient of the leaf  $G_j$  is positive, it indicates that the current prediction is underestimated, and thus a negative update should be applied. The denominator term,  $H_j + \lambda$ , acts as a step-size regulator, analogous to a confidence factor[39]. Substituting the solution back into Equation (12), we obtain the minimized loss value,

$$\tilde{\mathcal{L}}^{(t)}(q) = -\frac{1}{2} \sum_{j=1}^T \frac{G_j^2}{H_j + \lambda} + \gamma T, \quad (15)$$

this equation is referred to as the structure score function. A smaller value of this objective function indicates a better tree fit. Finally, when splitting a leaf node into left and right child nodes ( $I_L$  and  $I_R$ ), with the original unsplit node denoted as  $I$ , the split gain is calculated as follows  $I = I_L \cup I_R$ , Losses before the split

$$\text{Loss}_{\text{before}} = -\frac{1}{2} \frac{(G_L + G_R)^2}{H_L + H_R + \lambda}, \quad (16)$$

the loss of separation is given by

$$\text{Loss}_{\text{after}} = -\frac{1}{2} \left( \frac{G_L^2}{H_L + \lambda} + \frac{G_R^2}{H_R + \lambda} \right), \quad (17)$$

The difference between them represents the splitting gain, from which a penalty term for the newly added leaf is subtracted. Therefore, the core metric XGBoost uses to select a split point can be expressed as [34]

$$\text{Gain}_{\text{split}} = \frac{1}{2} \left[ \frac{G_L^2}{H_L + \lambda} + \frac{G_R^2}{H_R + \lambda} - \frac{(G_L + G_R)^2}{H_L + H_R + \lambda} \right] - \gamma. \quad (18)$$

## 2.2 Bayesian Hyperparameter Optimization and BayesSearchCV

In this study, we employ Bayesian hyperparameter optimization to enhance the performance and generalization ability of our XGBoost model for predicting the logarithm of nuclear half-life. This approach provides a systematic strategy for tuning key parameters, offering greater efficiency than traditional methods like Grid Search or Random Search. Bayesian optimization works by constructing a probabilistic surrogate model-typically based on Gaussian processes or tree-based regressors-to approximate the objective function.

During optimization, an acquisition function (such as Expected Improvement) guides the search by determining the next sampling point at each iteration. It balances predicted performance against model uncertainty, directing the search toward regions likely to yield improvement and thereby striking an efficient balance between exploration and exploitation.

Each iteration involves updating the surrogate model with accumulated evaluation data and selecting the next hyperparameter set based on the highest expected improvement in performance. This iterative process enables progressive convergence toward the global optimum within a limited evaluation budget [40-42].

For this study, we configured Bayesian optimization with 80 search iterations (`n_iter`) and 10 cross-validation folds (`cv`). This setup facilitated thorough exploration of the high-dimensional hyperparameter space while maintaining computational feasibility and balancing model stability against evaluation accuracy. During each iteration, the algorithm updated the hyperparameters' posterior distribution using accumulated evaluation data, guiding the selection of the next parameter set to efficiently balance global exploration and local exploitation.

This optimization strategy significantly enhanced the model's validation performance while mitigating overfitting risk. These improvements established a robust foundation for subsequent interpretability analysis.

We defined the search space for eight key XGBoost regression hyperparameters,

as summarized in Table 1.

**Table 1** Hyperparameter search space for XGBoost model optimization using Bayesian approach

Name	Type	Search Range
n_estimators	Integer	[1000, 1200]
max_depth	Integer	[5, 10]
learning_rate	Real (log-uniform)	[0.01, 0.1]
subsample	Real	[0.6, 0.8]
colsample_bytree	Real	[0.6, 0.8]
gamma	Real	[0, 0.5]
reg_alpha	Real	[0.5, 2]
reg_lambda	Real	[0.5, 2]

In hyperparameter optimization, the Integer type defines discrete-valued parameters sampled uniformly from a specified integer range. This applies to parameters like the number of boosting rounds (n\_estimators) and maximum tree depth (max\_depth), where only integer values are meaningful.

Conversely, the Real type applies to continuous-valued parameters sampled uniformly from a defined real interval. This is suitable for hyperparameters requiring fine-grained tuning, such as regularization strengths and sampling ratios.

For the particularly sensitive real-valued learning rate (learning\_rate), we employed log-uniform sampling. This technique samples parameters uniformly in logarithmic space, enabling efficient exploration across multiple orders of magnitude. Log-uniform sampling avoids bias toward larger values and proves especially advantageous when the parameter's optimal scale is unknown a priori.

### 2.3 Data input and feature engineering construction

All nuclear properties used in this study-including proton number, neutron number, decay energy, spin-parity information, and half-life data were obtained from Refs. [25-27]. This research is structured in two main phases: first predicting decay energies, then utilizing these predicted energies for half-life estimation.

#### (1) Decay Energy Prediction

To accurately predict decay energies, six nuclear features were selected as input parameters for the model, as summarized in Table 2.

**Table 2** Decay Energy Prediction-Related Features

Name	relevant calculations
Mass number	A
Proton number	Z
Neutron number	N
Proton-neutron ratio	Z/N
relative neutron excess	(N-Z)/A

These variables represent fundamental nuclear properties and nucleon configurations within the atomic nucleus. As critical determinants of binding energy

and decay behavior, they exhibit strong nonlinear correlations with decay energy – a relationship substantiated by both liquid-drop and shell models [43-44]. Maintaining consistent input features across nuclear mass regions (light, heavy, and superheavy nuclei) enhances the model's generalization capability when applied to our dataset of 1,623 nuclides with positive decay energies ( $Q > 0$ ).

Using a 9:1 train-test split, we randomly partitioned 326 nuclides for testing. The model demonstrated strong predictive performance, with detailed results and SHAP interpretability analysis presented in the following section.

## (2) Half-life Prediction

This stage represents the core methodology of our study. We incorporate the decay energy predictions from the previous step as key input features for half-life estimation. The selected feature parameters are summarized in Table 3.

**Table 3** Relevant Features for Half-Life Prediction

Name	relevant calculations
Mass number of the parent nucleus	$A_1$
Proton number of the parent nucleus	$Z_1$
Neutron number of the parent nucleus	$N_1$
total angular momentum transfer (parity not included)	$j=j_p+j_d$
Coefficient of the inverse square root of $Q_\alpha$	$1/\sqrt{Q_\alpha}$
minimum angular momentum	$l_{\min}$
Z1 magic number distance	$ Z_1 - \text{magic} _{\min}$
Even-odd property of Z1	If $Z_1 \% 2=0$ ;output 1,else 0
relative neutron excess of the parent nucleus	$\frac{N_1 - Z_1}{A_1}$
Neutron proton number ratio of the parent nucleus	$\frac{N_1}{Z_1}$

In addition to fundamental parent nucleus properties, we computed the minimum total angular momentum transfer ( $j_{\min}$ ) required for  $\alpha$ -decay. Derived from parent-daughter spin-parity coupling, this quantity critically governs hindrance factors and selection rules. It embodies the Geiger-Nuttall relationship between decay energy and half-life, aligning with semi-empirical models and experimental observations. Notably,  $j_{\min}$  demonstrates the highest feature importance in our model.

The relative neutron excess ( $\delta$ ) and neutron-to-proton ratio ( $N/Z$ ) reflect nucleon distribution asymmetry, indirectly indicating binding energy and stability. These correspond to the liquid-drop model's symmetry energy term and are particularly crucial for predicting decay behavior in nuclides far from stability.

We introduced the minimum proton magic number difference ( $\Delta Z_{\text{magic}}$ ) to quantify shell closure proximity—a key modulator of half-life through shell effects [45-46]. Proton magic numbers used were: 2, 8, 20, 28, 50, 82, 126.

Parent nucleus proton parity was included as a stability indicator. Even proton numbers favor spin-paired states, lowering total energy and enhancing stability, while odd-Z nuclei exhibit pairing energy loss and reduced stability [47].



Finally, the minimum orbital angular momentum ( $\ell_{\min}$ ) for  $\alpha$ -particle emission represents the lowest momentum transfer conserving total angular momentum and parity. Calculated via Eq. (18) [48], this feature significantly influences tunneling probability through the potential barrier.

$$l_{\min} = \begin{cases} \Delta_j & \text{for even } \Delta_j \text{ and } \pi_p = \pi_d \\ \Delta_j + 1 & \text{for even } \Delta_j \text{ and } \pi_p \neq \pi_d \\ \Delta_j & \text{for odd } \Delta_j \text{ and } \pi_p \neq \pi_d \\ \Delta_j + 1 & \text{for odd } \Delta_j \text{ and } \pi_p = \pi_d \end{cases}, \quad (18)$$

where  $\Delta_j = |j_p - j_d|$ .

The selection of these features is based on established physical models, enabling deeper insights into nuclear structural stability and decay mechanisms while significantly enhancing both the predictive performance and physical consistency of our half-life model.

For  $\alpha$ -decay half-life prediction, we selected 697 nuclides with decay energies  $Q_\alpha > 3.5$  MeV for model training. Using a 9:1 train-test split, detailed predictive results and SHAP interpretability analysis are presented in Section 4.

## 2.4 Empirical Formulas (Royer and Budaca)

In  $\alpha$ -decay half-life studies, simple-form empirical formulas are widely adopted for rapid estimation due to their computational efficiency. These models often serve as benchmarks for theoretical frameworks, typically incorporating nuclide classification schemes to enhance predictive accuracy.

For this work, we employ two widely-used and continuously refined empirical formulations: the Royer formula and the Budaca formula. We briefly introduce both in this section, where they will serve as comparative benchmarks in subsequent analyses.

### (1) Royer Formula

The Royer formula, originally proposed by G. Royer, derives from the liquid-drop model and is empirically fitted to experimental data [6-8]. This expression is applicable to nuclides across different proton-neutron parity combinations, with its basic form given by

$$\log_{10} [T_{1/2}(s)] = a + bA^{1/6}\sqrt{Z} + \frac{cZ}{\sqrt{Q_\alpha}}, \quad (19)$$

In order to extend the formula's applicability to decays involving non-zero angular momentum transfer, G. Royer and collaborators developed an angular momentum correction term. In this study, we employ the Royer formulation as presented in Ref. [13],

$$\log_{10} [T_{1/2}(s)] = a + bA^{1/6}\sqrt{Z} + \frac{cZ}{\sqrt{Q_\alpha}} + \frac{l(l+1)}{\sqrt{(A-4)(Z-2)} \cdot A^{-2/3}}, \quad (20)$$

here,  $A$  is the mass number of the parent nucleus,  $Z$  is the proton number, and  $Q_\alpha$  is the decay energy. The coefficients  $a$ ,  $b$ , and  $c$  are fitted parameters that vary depending on the even-odd nature of the proton and neutron numbers. The four corresponding parameter sets are summarized in Table 4.

**Table 4** Coefficients in the Royer Formula

Nuclei	a	b	c
e-e	-25.31	-1.1629	1.5864
e-o	-26.65	-1.0859	1.5848
o-e	-25.68	-1.1423	1.5920
o-o	-20.48	-1.1130	1.6971

## (2) Budaca Formula

The Budaca formula accounts for detailed nuclear structural effects and angular momentum hindrance, which enables targeted enhancement of predictive accuracy for nuclei in odd-mass quantum states. By incorporating structure-dependent correction terms, it achieves wider applicability across nuclide categories [9],

$$\log_{10} [T_{1/2}(s)] = A \cdot \chi \left(1 - D_1 \cdot \eta \cdot \frac{\chi^2}{\rho^2}\right) + B \cdot \rho \left(1 + D_2 \cdot \eta \cdot \frac{\chi^2}{\rho^2}\right) + C, \quad (21)$$

We employ a modified Budaca formulation incorporating both angular momentum barrier corrections and symmetry energy terms as a comparative benchmark[10].

$$\begin{aligned} \log_{10} [T_{1/2}(s)] = & A \cdot \chi \left(1 - D_1 \cdot \eta \cdot \frac{\chi^2}{\rho^2}\right) + B \cdot \rho \left(1 + D_2 \cdot \eta \cdot \frac{\chi^2}{\rho^2}\right) \\ & + C + \frac{E \cdot l(l+1)}{\mu \cdot \sqrt{Z_\alpha Z_d (A_\alpha^{1/3} + A_d^{1/3})}} + F \cdot I + G \cdot I^2, \end{aligned} \quad (22)$$

with

$$\chi = Z_\alpha Z_d \sqrt{\frac{A_\alpha A_d}{(A_\alpha + A_d) Q_\alpha}}, \quad (23)$$

$$\rho = \sqrt{\frac{Z_\alpha Z_d A_\alpha A_d (A_\alpha^{1/3} + A_d^{1/3})}{A_\alpha + A_d}}, \quad (24)$$

$$\eta = A_\alpha^{1/3} + A_d^{1/3}, \quad (25)$$

$$I = (N - Z)/A. \quad (26)$$

Among the formula terms,  $Z_\alpha=2$  and  $A_\alpha=4$  represent the proton number and mass number of the emitted  $\alpha$ -particle, respectively. The Budaca formula's fitting coefficients vary according to the parent nucleus's proton-neutron even-odd parity combinations, corresponding to the four distinct cases listed in Table 5.

**Table 5** Coefficients in the Budaca Formula

Nuclei	A	D <sub>1</sub>	B	D <sub>2</sub>	C	E	F	G
e-e	0.41560	0.00042	0.41702	0.00165	23.12760	0	13.07393	46.21203
e-o	-0.31757	0.02123	0.22397	0.20732	-0.69503	30.01541	2.42445	47.15330
o-e	-0.10096	0.04269	0.23619	0.14041	-8.21459	27.06010	15.69965	-2.41994
o-o	-0.16055	0.02523	0.22103	0.15424	-5.45713	20.77405	12.01992	17.81946

Both empirical formulas have been extensively validated in  $\alpha$ -decay studies. While they cannot fully capture all microscopic mechanisms, they

provide foundational reference frameworks for understanding systematic nuclear decay trends. Building on this, we subsequently generate half-life predictions using these empirical models and perform a comprehensive comparative analysis against our machine learning model's results.

### III. NUMERICAL RESULTS

To evaluate the predictive performance of our XGBoost model for decay energy, we show representative samples from the training dataset comparing true versus predicted values in Table 6.

**Table 6** Summary of Decay Energy Prediction Results (Test Set)

A	Z	Q_exp(MeV)	Q_XGB(MeV)	Absolute error
130	58	0.822	0.848	0.026
166	75	5.519	5.486	0.033
197	87	7.896	7.877	0.019
234	93	5.356	5.521	0.165
179	73	2.383	2.370	0.013
228	95	8.392	8.343	0.049
286	113	9.790	9.822	0.032
195	85	7.344	7.379	0.035
207	88	7.273	7.332	0.059
146	66	1.980	1.990	0.010
186	77	3.849	3.776	0.073
259	105	9.619	9.443	0.176
194	77	0.626	0.595	0.031
111	52	2.500	2.368	0.132
172	78	6.463	6.555	0.092
170	74	4.143	4.159	0.015
179	80	6.351	6.398	0.047
145	66	2.557	2.486	0.071
256	102	8.582	8.496	0.086

**Table 6** continued

A	Z	Q_exp(MeV)	Q_XGB(MeV)	Absolute error
148	66	1.475	1.785	0.310
149	63	2.401	2.577	0.176
144	61	0.845	0.843	0.003
143	67	3.658	3.551	0.107
228	88	4.070	4.036	0.034
269	109	10.480	10.464	0.016
157	68	3.305	3.277	0.027
244	97	6.779	6.618	0.161
241	93	4.363	4.413	0.051
118	57	2.641	2.825	0.184
281	112	10.430	10.441	0.011
170	78	6.707	6.785	0.077

150	61	0.651	0.858	0.207
219	82	1.085	0.828	0.257
172	75	4.402	4.458	0.056
111	53	3.275	3.239	0.036
128	59	1.503	1.582	0.079
256	105	9.336	9.421	0.085
265	109	11.120	11.181	0.061
221	91	9.248	9.259	0.011
232	87	1.768	2.045	0.277
228	92	6.800	6.906	0.107
186	76	2.821	2.980	0.158
228	91	6.265	6.181	0.084
205	86	6.386	6.522	0.136
280	113	11.428	11.265	0.163
159	67	1.496	1.620	0.124
192	85	7.696	7.674	0.022
167	68	0.667	0.627	0.040
109	54	4.217	4.351	0.134
146	68	3.373	3.438	0.065
111	55	4.105	4.166	0.061
255	102	8.428	8.468	0.040
173	72	2.539	2.558	0.019
198	85	6.889	6.852	0.037
243	96	6.169	6.009	0.160
178	82	7.789	7.508	0.282
118	52	0.444	0.612	0.168
218	89	9.384	9.325	0.059
253	100	7.198	7.288	0.090
217	82	1.635	1.737	0.102
160	70	3.624	3.450	0.174

**Table 6** continued

<b>A</b>	<b>Z</b>	<b>Q_exp(MeV)</b>	<b>Q_XGB(MeV)</b>	<b>Absolute error</b>
135	65	3.986	3.955	0.031
160	67	1.284	1.320	0.037
234	94	6.310	6.185	0.125
172	72	2.753	2.671	0.081
188	84	8.082	7.876	0.206
223	91	8.343	8.389	0.046
239	90	2.945	2.998	0.053
117	52	0.808	0.818	0.010
238	90	3.169	3.161	0.008
118	56	2.461	2.193	0.268
202	80	0.134	0.329	0.196
191	85	7.822	7.837	0.014

134	60	1.352	1.121	0.231
267	105	7.920	8.162	0.242
243	94	4.757	4.731	0.026
161	71	3.722	3.914	0.192
244	94	4.666	4.529	0.136
188	79	4.815	4.399	0.415
176	76	4.541	4.548	0.007
154	64	0.920	0.659	0.261
164	67	0.431	0.620	0.189
123	59	2.365	2.293	0.072
146	61	1.907	1.867	0.040
269	110	11.510	11.335	0.175
186	73	0.738	0.554	0.184
144	68	3.797	4.141	0.344
239	91	3.555	3.537	0.018
285	114	10.560	10.667	0.107
162	76	6.768	6.681	0.086
190	83	6.862	6.986	0.124
181	71	0.347	0.313	0.034
212	86	6.385	6.551	0.166
237	98	8.220	8.102	0.118
208	80	1.930	1.573	0.357
209	88	7.143	6.979	0.164
277	112	11.622	11.736	0.114
212	85	7.817	8.263	0.446
144	60	1.901	1.652	0.250
221	86	6.163	6.116	0.047
161	69	2.509	2.680	0.171
234	90	3.672	3.645	0.027
192	80	3.385	3.530	0.145

**Table 6** continued

<b>A</b>	<b>Z</b>	<b>Q_exp(MeV)</b>	<b>Q_XGB(MeV)</b>	<b>Absolute error</b>
115	53	2.074	1.938	0.136
293	117	11.320	11.370	0.050
171	74	3.957	3.935	0.022
160	74	6.066	5.992	0.073
156	70	4.810	4.644	0.166

To evaluate our model's performance in predicting decay energy, we conducted quantitative evaluations on both training and testing datasets; results are summarized in Table 7.

**Table 7** Evaluation Metrics Analysis for Decay Energy Prediction

<b>Type</b>	<b><math>R^2</math></b>	<b>MSE</b>	<b>RMSE</b>	<b>MAE</b>
-------------	-------------------------	------------	-------------	------------

<b>Training Set</b>	0.9999	0.0010	0.0310	0.0236
<b>Test Set</b>	0.9971	0.0261	0.1617	0.1228

The results demonstrate that the model exhibits excellent fitting accuracy on the training set and maintains strong predictive performance on the testing set, indicating good generalization ability. Although the error on the test set is slightly higher, it remains at a low level, suggesting that the model handles unseen data effectively and provides a reliable input foundation for subsequent half-life predictions. To identify the contribution of various nuclear structure features to decay energy prediction, we conducted a feature importance analysis using the SHAP framework. The results are illustrated in Figure 1.

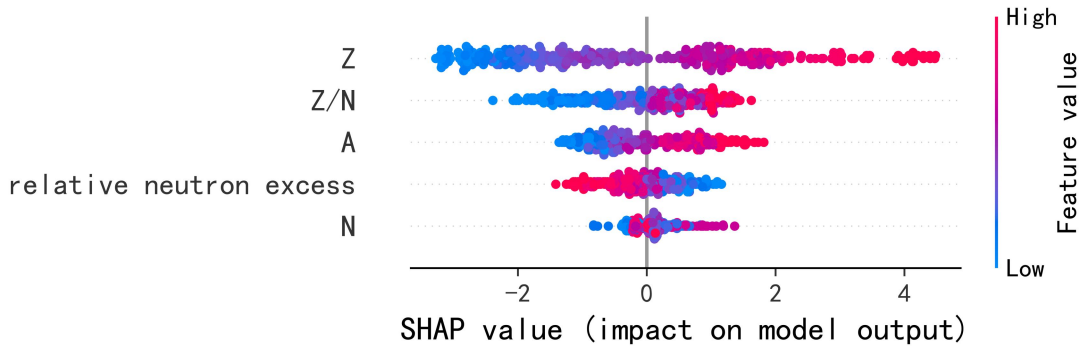


**Figure 1** SHAP summary plot showing the feature importance distribution in the decay energy prediction model. The horizontal axis represents SHAP values, indicating the impact of each feature on the model output per sample. Each dot corresponds to a single prediction instance, colored according to the feature value from low (blue) to high (red)

As shown in Figure 1, proton number ( $Z$ ) exhibits the strongest influence on model outputs. Higher  $Z$  values correspond to predominantly positive SHAP values, indicating that increased proton counts generally elevate predicted decay energy.

The next most impactful features-proton-to-neutron ratio ( $Z/N$ ) and mass number ( $A$ )-demonstrate strong nonlinear relationships with predictions, suggesting more complex governing mechanisms.

High relative neutron excess correlates with lower predicted decay energies, whereas near-symmetric  $N \approx Z$  configurations contribute positively. This reveals the model's capture of fundamental nuclear physics: nuclei near the valley of stability exhibit higher decay energies, while neutron-rich systems show reduced decay energy. Neutron number ( $N$ ) exhibits weaker influence overall, though marginal effects emerge at extreme values.

To further assess generalization capability, we compare predicted half-lives against Royer and Budaca empirical formulas. This validation is performed on both a training subset (Table 7) and the full test set (Table 8), evaluating model performance on known data versus extrapolation to novel cases..

**Table 7:** Partial half-life prediction results on the training set using the XGBoost model, including the

ground truth, predicted values, and calculated values from Royer and Budaca empirical formulas.

<b>nuclide</b>	<b><math>Q_\alpha</math>(MeV)</b>	<b>logT_exp</b>	<b>logT_XGB</b>	<b>logT_Royer</b>	<b>logT_Budaca</b>
<b>137Gd</b>	3.266	0.342	0.328	13.261	12.291
<b>160Yb</b>	3.470	2.459	2.479	11.632	11.694
<b>153Dy</b>	3.497	4.364	4.247	8.882	8.994
<b>151Er</b>	3.531	1.371	1.416	13.491	13.003
<b>166Hf</b>	3.544	2.609	2.607	12.228	12.319
<b>158Tm</b>	3.558	2.378	2.407	20.108	10.966
<b>206Bi</b>	3.560	5.732	5.789	37.717	27.085
<b>174W</b>	3.564	3.313	3.202	13.240	13.358
<b>173W</b>	3.601	2.641	2.708	13.098	13.914
<b>211Pb</b>	3.602	3.336	3.291	17.830	20.649
<b>110I</b>	3.608	-0.174	-0.265	11.012	1.804
<b>231Ac</b>	3.608	2.653	2.710	22.221	25.816
<b>114Ba</b>	3.620	-0.387	-0.409	2.222	1.455
<b>150Tb</b>	3.622	4.098	4.122	18.564	8.705
<b>198Pb</b>	3.632	3.937	4.059	17.526	17.685
<b>238Pa</b>	3.654	2.140	2.002	37.071	30.654
<b>242U</b>	3.657	3.003	3.214	23.162	23.064
<b>178Re</b>	3.660	2.899	3.057	23.187	14.618
<b>234Th</b>	3.668	6.319	6.202	21.855	21.805
<b>191Hg</b>	3.701	3.468	3.385	15.941	17.683
<b>145Er</b>	3.706	-0.046	-0.048	17.389	16.027
<b>237Pa</b>	3.710	2.718	2.623	22.429	26.328
<b>181Os</b>	3.713	3.803	3.756	13.342	14.469
<b>233Th</b>	3.729	3.117	3.174	23.257	27.435
<b>205Bi</b>	3.730	6.110	5.962	25.644	25.359

**Table 7** continued

<b>nuclide</b>	<b><math>Q_\alpha</math>(MeV)</b>	<b>logT_exp</b>	<b>logT_XGB</b>	<b>logT_Royer</b>	<b>logT_Budaca</b>
<b>177Re</b>	3.733	2.924	2.907	12.676	13.289
<b>165Hf</b>	3.734	1.881	1.942	12.523	12.690
<b>152Dy</b>	3.747	3.933	3.957	6.956	7.014
<b>193Tl</b>	3.747	3.113	3.090	16.221	17.719
<b>185Ir</b>	3.768	4.715	4.618	14.103	14.821
<b>169Ta</b>	3.775	2.468	2.448	12.882	12.865
<b>236Pa</b>	3.793	2.737	2.779	32.420	27.045
<b>186Ir</b>	3.806	4.777	4.750	24.845	15.796
<b>187Ir</b>	3.822	4.577	4.678	14.724	15.113
<b>180Os</b>	3.827	3.111	3.188	12.234	12.359
<b>152Tm</b>	3.840	0.716	0.751	38.515	21.243
<b>172W</b>	3.841	2.598	2.571	10.996	11.106
<b>226Rn</b>	3.843	2.647	2.792	17.667	17.496
<b>189Pt</b>	3.851	4.593	4.581	15.037	16.152
<b>150Lu</b>	3.858	-1.347	-1.318	20.936	10.860

<b>184Ir</b>	3.862	4.046	3.985	28.289	17.468
<b>110Xe</b>	3.866	-1.032	-1.071	-0.445	-1.179
<b>190Au</b>	3.884	3.410	3.524	32.116	20.327
<b>230Ac</b>	3.891	2.086	2.123	30.641	24.387
<b>161Lu</b>	3.895	1.886	1.798	9.146	9.301
<b>197Pb</b>	3.918	2.687	2.768	15.287	17.167
<b>155Ta</b>	3.934	-2.538	-2.513	10.296	10.808
<b>159Yb</b>	3.943	2.016	2.001	9.784	9.708
<b>157Tm</b>	3.953	2.338	2.172	16.156	14.326
<b>176Re</b>	3.955	2.502	2.430	20.701	11.889
<b>135Tb</b>	3.962	-3.027	-2.839	8.927	8.492
<b>112Cs</b>	3.963	-3.312	-3.216	8.897	0.250
<b>183Ir</b>	3.964	3.542	3.551	12.561	13.126
<b>164Hf</b>	3.965	2.045	2.000	8.967	9.037
<b>228Ra</b>	3.979	8.258	7.995	17.716	17.636
<b>154Ho</b>	3.979	2.849	2.909	15.432	6.276
<b>243Np</b>	3.980	2.045	2.016	22.599	25.966
<b>171W</b>	4.001	2.157	2.251	9.973	10.489
<b>175Re</b>	4.013	2.548	2.465	11.084	11.397
<b>204Bi</b>	4.031	4.609	4.651	33.244	21.914
<b>219Ra</b>	8.191	-2.046	-2.045	-1.326	-1.712
<b>222Th</b>	8.223	-2.706	-2.693	-2.667	-2.607
<b>184Bi</b>	8.224	-1.886	-1.906	15.709	2.197
<b>247Fm</b>	8.236	1.491	1.457	6.475	5.651
<b>212At</b>	8.258	-0.503	-0.604	12.780	0.594
<b>254No</b>	8.266	1.709	1.527	1.416	1.428
<b>213Rn</b>	8.284	-1.713	-1.581	4.169	2.489

Table 7 continued

nuclide	$Q_\alpha(\text{MeV})$	logT_exp	logT_XGB	logT_Royer	logT_Budaca
<b>215Pa</b>	8.287	-1.854	-1.946	-2.025	-1.941
<b>240Es</b>	8.307	0.826	0.659	15.312	4.014
<b>223Pa</b>	8.341	-2.276	-2.220	-2.351	-2.443
<b>211Pa</b>	8.346	-2.420	-2.460	-2.121	-1.955
<b>213Pa</b>	8.356	-2.276	-2.222	-2.192	-2.074
<b>212Pa</b>	8.378	-2.301	-2.214	6.948	-2.071
<b>246Fm</b>	8.381	0.185	0.102	0.379	0.431
<b>253No</b>	8.403	1.985	2.068	2.039	2.352
<b>220Ac</b>	8.411	-1.578	-1.611	7.397	-2.042
<b>249Md</b>	8.434	1.408	1.440	2.417	2.410
<b>256No</b>	8.461	0.467	0.380	0.723	0.702
<b>217Pa</b>	8.463	-2.432	-2.396	-2.592	-2.579
<b>255No</b>	8.467	2.325	2.384	8.900	7.451
<b>257No</b>	8.482	1.389	1.355	2.724	2.755
<b>262Rf</b>	8.488	-1.328	-1.358	1.320	1.282



<b>216U</b>	8.536	-2.347	-2.404	-2.677	-2.542
<b>252No</b>	8.559	0.389	0.316	0.484	0.519
<b>244Fm</b>	8.571	-2.506	-2.277	-0.193	-0.121
<b>255Lr</b>	8.580	1.493	1.431	6.156	5.104
<b>214Fr</b>	8.607	-2.260	-2.350	12.491	0.258
<b>224U</b>	8.612	-3.402	-3.528	-3.064	-2.972
<b>221Th</b>	8.621	-2.762	-2.710	-1.814	-2.226
<b>247Md</b>	8.766	0.079	0.082	1.396	1.295
<b>266Sg</b>	8.767	-0.469	-0.392	1.119	1.091
<b>218U</b>	8.778	-3.201	-3.137	-3.414	-3.283
<b>256Lr</b>	8.823	1.446	1.396	10.412	1.405
<b>256Rf</b>	8.890	-2.170	-1.875	0.142	0.183
<b>215Ra</b>	8.906	-2.775	-2.848	3.141	1.436
<b>260Rf</b>	8.909	-1.664	-1.663	0.003	-0.009
<b>253Lr</b>	8.927	-0.187	-0.241	0.045	0.488
<b>257Lr</b>	9.007	-0.693	-0.531	2.760	2.156
<b>255Rf</b>	9.068	0.223	0.124	0.698	0.802
<b>257Rf</b>	9.089	0.653	0.583	7.647	6.016
<b>270Hs</b>	9.118	0.881	0.723	0.704	0.684
<b>258Rf</b>	9.175	-2.008	-1.988	-0.763	-0.750
<b>264Sg</b>	9.198	-1.222	-1.221	-0.190	-0.194
<b>286Cn</b>	9.212	2.820	2.659	1.640	1.521
<b>216Ac</b>	9.236	-3.444	-3.288	11.453	-0.765
<b>253Rf</b>	9.268	-1.987	-1.951	4.659	3.578
<b>251Lr</b>	9.419	-1.613	-1.593	-1.368	-1.055
<b>258Db</b>	9.445	0.318	0.182	10.229	0.627
<b>262Sg</b>	9.565	-1.943	-1.926	-1.225	-1.207

Table 7 continued

nuclide	$Q_\alpha(\text{MeV})$	logT_exp	logT_XGB	logT_Royer	logT_Budaca
<b>284Cn</b>	9.617	-0.917	-0.678	0.432	0.341
<b>258Sg</b>	9.684	-2.569	-2.551	-1.481	-1.422
<b>268Hs</b>	9.757	-0.398	-0.469	-1.147	-1.148
<b>290Fl</b>	9.851	1.279	1.265	0.366	0.254
<b>260Sg</b>	9.893	-2.316	-2.355	-2.094	-2.057
<b>266Hs</b>	10.322	-2.527	-2.495	-2.629	-2.612
<b>286Fl</b>	10.367	-0.917	-0.912	-1.011	-1.070
<b>261Bh</b>	10.483	-1.932	-1.874	-1.448	-1.662
<b>264Hs</b>	10.582	-3.201	-3.276	-3.251	-3.215
<b>292Lv</b>	10.810	-1.893	-1.994	-1.600	-1.683
<b>270Ds</b>	11.123	-3.721	-3.666	-3.994	-3.979
<b>294Og</b>	11.873	-3.237	-3.025	-3.558	-3.618

**Table 8:** Complete half-life prediction results on the test set using the XGBoost model, including ground truth, predicted values, and the Royer and Budaca empirical formula values, aiming to evaluate

the model's generalization performance on unseen nuclides.

nuclide	$Q_\alpha(\text{MeV})$	logT_exp	logT_XGB	logT_Royer	logT_Budaca
229Ra	3.628	2.380	2.728	21.910	26.068
168Ta	3.767	2.079	2.283	22.710	13.043
240U	4.015	4.706	5.513	19.724	19.634
192Tl	4.038	2.760	3.022	25.508	16.491
235Pa	4.049	3.166	3.202	19.774	22.825
179Os	4.150	2.577	2.883	10.003	10.748
151Dy	4.164	3.033	3.254	4.251	4.294
146Tm	4.171	-0.810	-0.816	31.563	16.183
165Ta	4.279	1.491	1.471	16.087	14.435
229Ac	4.379	3.575	4.335	15.907	17.998
191Tl	4.401	2.502	2.629	19.301	18.109
170Re	4.770	0.964	1.081	20.685	9.253
169Re	5.037	0.908	0.923	4.260	4.404
173Os	5.041	1.350	1.407	4.651	4.820
245Am	5.121	3.867	3.192	13.304	15.628
223Rn	5.181	3.164	2.617	10.057	11.099
186Hg	5.246	1.918	1.900	5.251	5.383
154Yb	5.496	-0.388	0.227	-0.469	-0.485
203Po	5.553	3.343	3.646	7.338	7.720
165Re	5.681	0.204	0.148	9.572	7.914
202Po	5.710	3.427	3.806	4.639	4.762
190Pb	5.750	1.851	1.842	3.690	3.823
172Ir	5.929	0.643	0.351	18.422	5.938
223Ra	6.032	5.995	4.371	6.658	7.133
246Bk	6.058	5.192	6.052	20.515	11.962

Table 8 continued

nuclide	$Q_\alpha(\text{MeV})$	logT_exp	logT_XGB	logT_Royer	logT_Budaca
253Cf	6.129	6.186	4.713	14.225	14.980
184Tl	6.226	0.978	1.049	11.264	1.914
236Am	6.296	2.334	3.090	17.324	8.772
248Cf	6.385	7.460	6.633	7.360	7.337
179Hg	6.398	0.021	0.101	0.416	0.361
212Rn	6.424	3.157	2.991	2.183	2.249
182Tl	6.461	0.279	0.486	13.005	2.526
176Au	6.471	0.021	0.083	10.445	0.707
180Tl	6.567	0.037	-0.008	10.984	1.188
172Pt	6.603	-1.011	-0.776	-1.374	-1.365
251Es	6.609	5.075	5.566	7.079	8.394
163Os	6.660	-2.237	-2.785	-2.105	-2.311
191Bi	6.735	1.093	1.218	8.346	6.411
173Au	6.830	-1.580	-1.432	-1.524	-1.256
216Po	6.866	-0.842	-0.938	-0.562	-0.670

<b>194Po</b>	6.984	-0.407	0.078	-0.529	-0.394
<b>241Bk</b>	7.018	2.441	3.196	5.062	5.710
<b>161Os</b>	7.052	-3.194	-3.061	-3.374	-3.586
<b>217At</b>	7.189	-1.487	-1.039	-1.026	-1.342
<b>181Pb</b>	7.240	-1.444	-1.238	-0.128	-0.542
<b>192Po</b>	7.324	-1.492	-0.928	-1.671	-1.549
<b>251Fm</b>	7.398	4.281	4.421	4.853	5.663
<b>206Ra</b>	7.436	-0.620	-0.856	-0.627	-0.486
<b>193At</b>	7.585	-1.553	-1.467	6.137	4.243
<b>192At</b>	7.666	-1.056	-1.681	21.893	6.483
<b>226U</b>	7.691	-0.573	-0.696	-0.213	-0.143
<b>199Fr</b>	7.804	-2.347	-2.110	-1.846	-1.683
<b>255Md</b>	7.869	3.210	3.191	4.261	4.453
<b>216At</b>	7.927	-3.523	-3.012	5.620	-2.907
<b>212Th</b>	7.980	-1.499	-1.517	-1.706	-1.568
<b>248Fm</b>	7.991	1.538	1.627	1.660	1.691
<b>242Fm</b>	8.718	-3.097	-1.912	-0.612	-0.522
<b>251No</b>	8.739	-0.097	-0.234	0.487	0.749
<b>257Db</b>	9.251	-0.174	-0.413	4.772	3.650
<b>217Th</b>	9.409	-3.595	-2.988	2.509	0.781
<b>259Sg</b>	9.773	-0.398	0.152	0.357	0.035
<b>288Fl</b>	10.081	-0.194	-0.417	-0.259	-0.344
<b>290Lv</b>	11.029	-2.081	-1.796	-2.121	-2.179

Similarly, to enable intuitive evaluation of prediction quality, we present quantitative results for half-life predictions across both training and test sets in Table 9.

**Table 9** Evaluation Metrics Analysis for Half-life Prediction

Type	$R^2$	MSE	RMSE	MAE
<b>Training Set</b>	0.9988	0.0079	0.0602	0.0712
<b>Test Set</b>	0.9610	0.2015	0.4807	0.3475

For the training set, the model achieves exceptional goodness-of-fit, successfully capturing complex nonlinear relationships within the data. Evaluation on the test set confirms strong generalization capability. While test set prediction errors are slightly higher than training errors, they remain within acceptable limits - indicating robust performance for unseen data.

To further validate performance, we compared test set predictions against two classical empirical formulas: Royer and Budaca. Royer yields MAE=6.6190 and RMSE=10.0704, while Budaca gives MAE=4.5359 and RMSE=7.1670. Both significantly exceed our model's errors (MAE=0.3475, RMSE=0.4807), demonstrating the machine learning approach's superior accuracy and reliability.

To enhance model interpretability and quantify feature contributions to half-life predictions, we conducted SHAP (SHapley Additive exPlanations) analysis. Results

are presented in Figure 2.

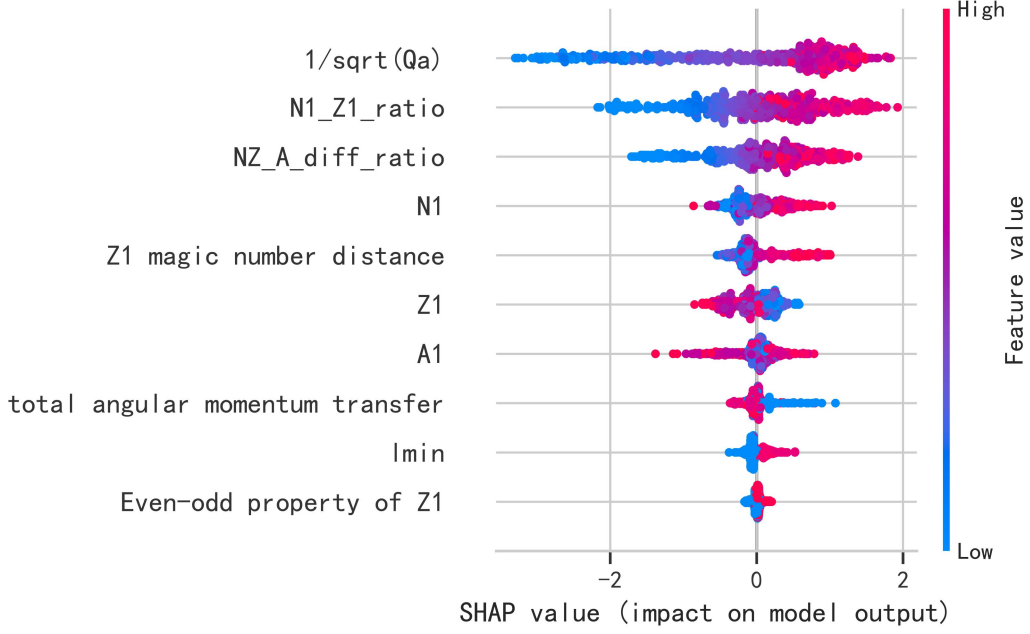


**Figure 2** SHAP summary plot showing the feature importance distribution in the half-life prediction model

As expected, decay energy ( $Q_\alpha$ ) exhibits the strongest positive contribution, reaffirming its decisive role in half-life prediction consistent with the Geiger-Nuttall law. Higher  $Q_\alpha$  corresponds to shorter half-lives ( $\log T_{1/2}$ ) due to increased penetration probability.

The neutron-to-proton ratio ( $N/Z$ ) and relative neutron excess ( $\delta$ ) reflect nucleon balance and its regulatory effect on nuclear stability. Both show strong contributions, indicating the critical influence of nucleon structure on decay kinetics.

Proximity to magic numbers ( $\Delta Z_{magic}$ ) markedly alters half-life, highlighting nuclear shell effects in  $\alpha$ -decay. SHAP distributions indicate that larger  $\Delta Z_{magic}$  values generally correspond to longer half-lives.

Angular momentum features ( $j_{min}$ ,  $\ell_{min}$ ) represent centrifugal barrier effects. Though their contributions are smaller than energy-related terms, they become prominent in cases with large spin mismatch.

Proton parity (even-odd  $Z$ ) shows minor average impact but exhibits significant shifts for specific nuclides, suggesting non-negligible effects through pairing energy mechanisms.

To visualize model performance, we plotted residuals of predicted vs. actual  $\log T_{1/2}$  with 95% confidence intervals from linear regression (Figures 3-5). These demonstrate fitting performance on training data and evaluate model stability.

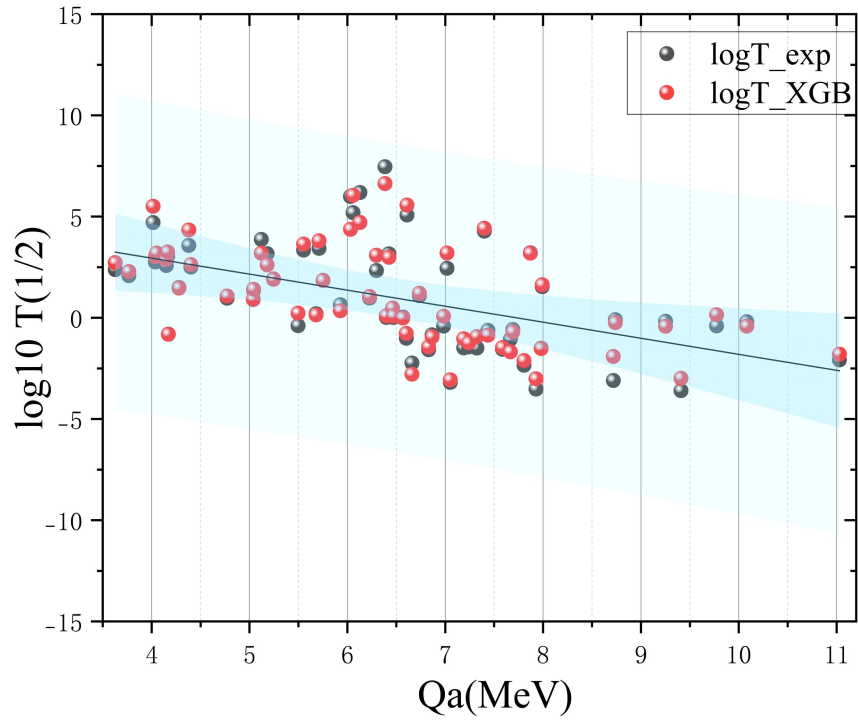


**Figure 3** Residual analysis between XGBoost-predicted values and experimental data

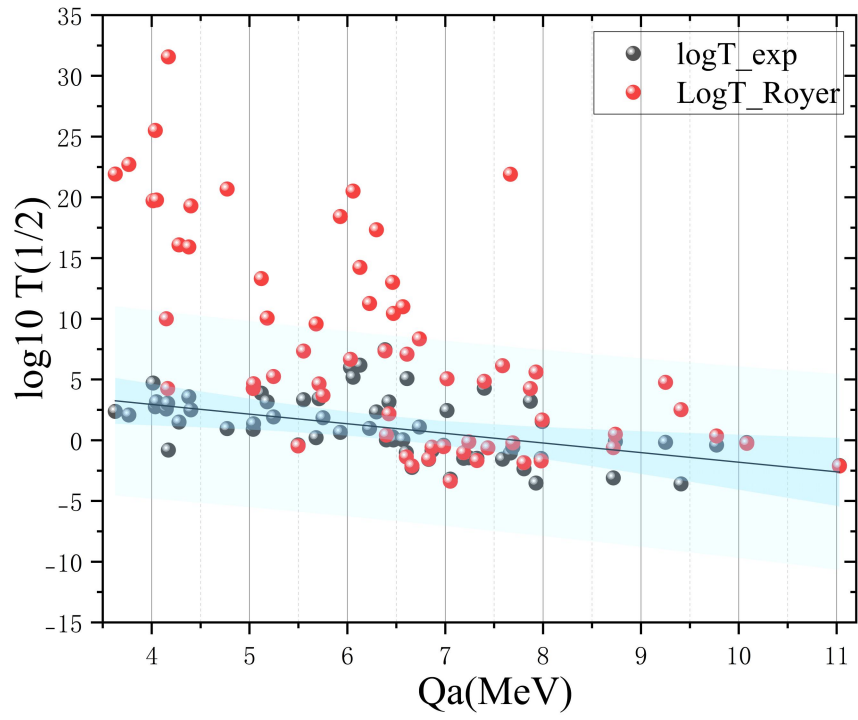


**Figure 4** Residual analysis between Royer formula results and experimental data

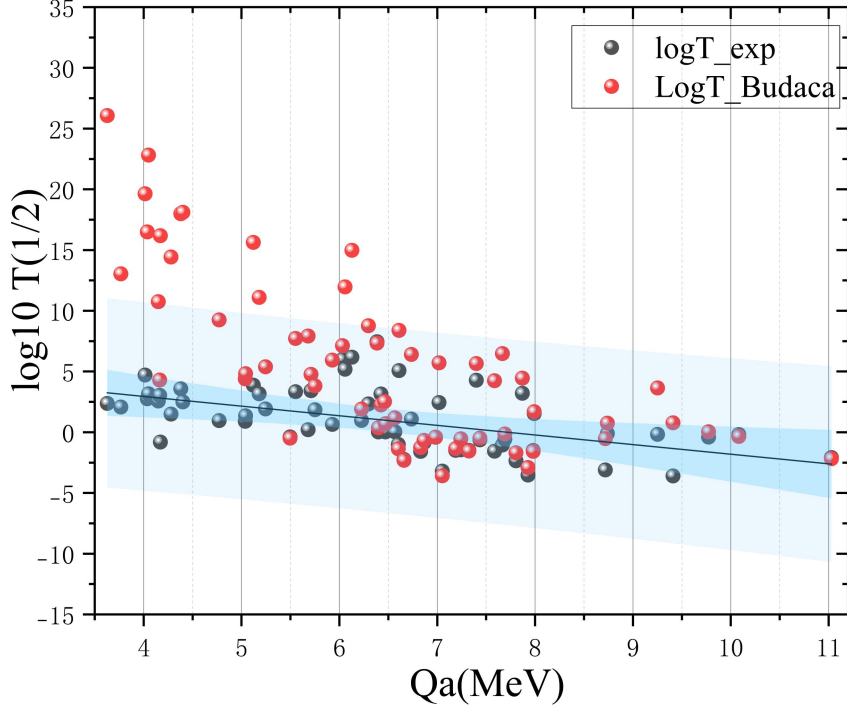


**Figure 5** Residual analysis between Budaca formula results and experimental data

As shown in Figures 3-5, the Royer and Budaca empirical formulas exhibit systematic deviations from experimental data. A significant portion of predicted values fall outside the 95% confidence intervals, particularly at low decay energies where discrepancies are most pronounced—indicating limited applicability in this regime. These deviations arise because traditional formulas inadequately account for: The strong sensitivity of penetration probability to  $Q_\alpha$ ; Nonlinear contributions from angular momentum barriers.

While accuracy improves slightly at higher energies, substantial deviations persist—especially for nuclei with complex structures or those far from stability.

Conversely, the XGBoost model demonstrates superior consistency across the entire energy spectrum. In low-energy regions, its predictions closely match experimental values with most points within confidence intervals, significantly enhancing accuracy. This robust performance reflects both strong nonlinear fitting capability and effective capture of key physical mechanisms: Exponential  $Q_\alpha$ -dependence of half-life; Penetration probability modulation by  $\ell_{\min}$  barriers; Localized nuclear shell effects.

In summary, XGBoost substantially outperforms empirical formulas in predictive accuracy, stability, and adaptability across energy domains, demonstrating both physical consistency and strong application potential for  $\alpha$ -decay modeling.

#### IV. CONCLUSION

This study develops an XGBoost-based predictive model for two fundamental  $\alpha$ -decay properties — decay energy and half-life — benchmarked against classical empirical formulas. By incorporating Bayesian hyperparameter optimization and systematically constructing nuclear structure features, our model demonstrates excellent predictive performance on both training and testing datasets. Particularly in the low decay-energy region, it exhibits enhanced fitting accuracy and reduced systematic deviations, effectively overcoming limitations of traditional formulas. Evaluation metrics (MAE/RMSE) significantly outperform those of Royer and Budaca formulations.

SHAP-based analysis confirms the model captures key  $\alpha$ -decay physics beyond numerical accuracy: Decay energy's decisive role (aligning with Geiger-Nuttall law); Reasonable representation of angular momentum barriers; Accurate reflection of proton/neutron structure and shell effects. These results demonstrate strong generalization capability and physical interpretability.

Our machine learning framework provides an efficient, reliable, and physically consistent tool for  $\alpha$ -decay prediction. Future work could extend this approach to other decay modes or incorporate additional experimental data to enhance adaptability-advancing theoretical support for nuclear structure studies and nuclide screening.

## V. ACKNOWLEDGEMENTS

This work is supported by Yunnan Provincial Science Foundation Project (No. 202501AT070067), Yunnan Provincial Xing Dian Talent Support Program (Young Talents Special Program), Kunming University Talent Introduction Research Project (No. YJL24019), Yunnan Provincial Department of Education Scientific Research Fund Project (No. 2025Y1055 and 2025Y1042), the Program for Frontier Research Team of Kunming University 2023, National Natural Science Foundation of China (No. 12063006), National College Student Innovation and Entrepreneurship Training Program (No. 202511393012, 202511393013, and 202511393016) , and Yunnan Province College Student Innovation and Entrepreneurship Training Program (No. S202511393003, S202511393043, and S202511393044).

## References

- [1] E. Rutherford and T. Royds, *Philosophical Magazine*, 17(98), 281-286 (1909).
- [2] E. Rutherford, *Philosophical Magazine*, 47(284), 109-163 (1899).
- [3] E. Rutherford and H. Geiger, *Proc. Roy. Soc. A*, 81(546), 141–161 (1908).
- [4] H. Geiger and J. M. Nuttall, *Philosophical Magazine*, 22(130), 613-621 (1911).
- [5] G. Gamow, *Zeitschrift für Physik*, 51(3), 204-212 (1928).
- [6] G. Royer, *Journal of Physics G: Nuclear and Particle Physics*, 26(8), 1149 (2000).
- [7] J. G. Deng, H. F. Zhang, and G. Royer, *Physical Review C*, 101(3), 034307 (2020).
- [8] D. Jianmin, Z. Hongfei, W. Yanzhao, Z. Wei, and L. Junqing, *Nuclear Physics A*, 832 (2010).

- [9] A. I. Budaca, R. Budaca, and I. Silisteanu, *Nuclear Physics A*, 951, 60-74 (2016).
- [10] D. T. Akrawy, A. I. Budaca, G. Saxena, and A. H. Ahmed, *The European Physical Journal A*, 58(8), 145 (2022).
- [11] C. Qi, F. R. Xu, R. J. Liotta, and R. Wyss, *Physical Review Letters*, 103 (7), 072501 (2009).
- [12] N. G. Kelkar and M. Nowakowski, *Physical Review C*, 89(1), 014602 (2014).
- [13] Y. Z. Wang, J. M. Dong, B. B. Peng, and H. F. Zhang, *Physical Review C*, 81(6), 067301 (2010).
- [14] X. Liu, J. D. Jiang, X. J. Wu, and X. H. Li, *Chinese Physics C*, 48(5), 054101 (2024).
- [15] M. R. Mumpower, T. M. Sprouse, A. E. Lovell, and A. T. Mohan, *Physical Review C*, 106(2), L021301 (2022).
- [16] W. He, Q. Li, Y. Ma, Z. Niu, J. Pei, and Y. Zhang, *Science China Physics, Mechanics & Astronomy*, 66(8), 282001 (2023).
- [17] P. P. Shinde and S. Shah, 2018 Fourth International Conference on Computing Communication Control and Automation (ICCUBEA), 1-6 (2018).
- [18] Y. LeCun, Y. Bengio, and G. Hinton, *Nature*, 521(7553), 436-444 (2015).
- [19] J. M. Zhang, M. Harman, L. Ma, and Y. Liu, *IEEE Transactions on Software Engineering*, 48(1), 1-36 (2020).
- [20] Z. Jin, M. Yan, H. Zhou, A. Cheng, Z. Ren, and J. Liu, *Physical Review C*, 108(1), 014326 (2023).
- [21] N. N. Ma, T. L. Zhao, W. X. Wang, and H. F. Zhang, *Physical Review C*, 107(1), 014310 (2023).
- [22] G. Saxena, P. K. Sharma, and P. Saxena, *Journal of Physics G: Nuclear and Particle Physics*, 48(5), 055103 (2021).
- [23] H. Q. You, Z. Z. Qu, R. H. Wu, H. Z. Su, and X. T. He, *Symmetry*, 14 (5), 1006 (2022).
- [24] C. Q. Li, C. N. Tong, H. J. Du, and L. G. Pang, *Physical Review C*, 105(6), 064306 (2022).
- [25] F. G. Kondev, M. Wang, W. J. Huang, S. Naimi, and G. Audi, *Chinese Physics C*, 45(3), 030001 (2021).
- [26] M. Wang, W. J. Huang, F. G. Kondev, G. Audi, and S. Naimi, *Chinese Physics C*, 45(3), 030003 (2021).
- [27] W. J. Huang, M. Wang, F. G. Kondev, G. Audi, and S. Naimi, *Chinese Physics C*, 45(3), 030002 (2021).
- [28] B. Cai, G. Chen, J. Xu, C. Yuan, C. Qi, and Y. Yao, *Physical Review C*, 101(5), 054304 (2020).
- [29] M. Hosseini-Tabatabaei, S. A. Alavi, and V. Dehghani, *Canadian Journal of Physics*, 99(1), 24-32 (2021).
- [30] H. F. Zhang and G. Royer, *Physical Review C*, 77(5), 054318 (2008).
- [31] V. Y. Denisov and A. A. Khudenko, *Physical Review C*, 79(5), 054614 (2009).
- [32] M. M. Ahsan, M. P. Mahmud, P. K. Saha, K. D. Gupta, and Z. Siddique,



- Technologies, 9(3), 52 (2021).
- [33] L. B. de Amorim, G. D. Cavalcanti, and R. M. Cruz, *Applied Soft Computing*, 133, 109924 (2023).
  - [34] T. Chen and C. Guestrin, *Proceedings of the 22nd ACM SIGKDD International Conference on Knowledge Discovery and Data Mining*, 785-794 (2016).
  - [35] S. M. Shree and M. Balasubramaniam, *The European Physical Journal A*, 61(2), 32 (2025).
  - [36] Y. Zhang and L. Chen, *Theoretical Economics Letters*, 11(2), 258-267 (2021).
  - [37] Z. H. Zhou, *Ensemble Methods: Foundations and Algorithms*, CRC Press (2025).
  - [38] J. H. Friedman, *Annals of Statistics*, 29(5), 1189-1232 (2001).
  - [39] X. Dong, T. Lei, S. Jin, and Z. Hou, *2018 IEEE 7th Data Driven Control and Learning Systems Conference (DDCLS)*, 854-859 (2018).
  - [40] J. Wu, X. Y. Chen, H. Zhang, L. D. Xiong, H. Lei, and S. H. Deng, *Journal of Electronic Science and Technology*, 17(1), 26-40 (2019).
  - [41] X. Wang, Y. Jin, S. Schmitt, and M. Olhofer, *ACM Computing Surveys*, 55(13s), 1-36 (2023).
  - [42] B. Bischl, M. Binder, M. Lang, T. Pielok, J. Richter, S. Coors, and M. Lindauer, *Wiley Interdisciplinary Reviews: Data Mining and Knowledge Discovery*, 13(2), e1484 (2023).
  - [43] G. Royer, *Nuclear Physics A*, 807(3-4), 105-118 (2008).
  - [44] H. Zhang, W. Zuo, J. Li, and G. Royer, *Physical Review C*, 74(1), 017304 (2006).
  - [45] H. Nakada, *Physical Review C*, 100(4), 044310 (2019).
  - [46] O. Sorlin and M. G. Porquet, *Progress in Particle and Nuclear Physics*, 61(2), 602-673 (2008).
  - [47] S. Amiel and H. Feldstein, *Physical Review C*, 11(3), 845 (1975).
  - [48] G. Saxena, A. Jain, and P. K. Sharma, *Physica Scripta*, 96(12), 125304 (2021).